Crystal structure of the complete integrin αVβ3 ectodomain plus an α/β transmembrane fragment

Jian-Ping Xiong,[1,2] Bhuvaneshwari Mahalingham,[1,2] Jose Luis Alonso,[1,2] Laura Ann Borrelli,[3] Xianliang Rui,[1,2] Saurabh Anand,[1,2] Bradley T. Hyman,[3] Thomas Rysiok,[4] Dirk Müller-Pompalla,[5] Simon L. Goodman,[6] and M. Amin Arnaout[1,2]

[1]Program in Leukocyte Biology and Inflammation and [2]Program in Structural Biology, Nephrology Division, Department of Medicine and [3]Institute for Neurodegenerative Disease, Massachusetts General Hospital, Harvard Medical School, Charlestown, MA 02129
[4]Biologicals: Protein and Cell Science, [5]Biologicals: Protein Purification, and [6]Therapeutic Area Oncology: Biochemistry and Cellular Pharmacology, Merck-Serono Research, 64293 Darmstadt, Germany

We determined the crystal structure of 1TM-αVβ3, which represents the complete unconstrained ectodomain plus short C-terminal transmembrane stretches of the αV and β3 subunits. 1TM-αVβ3 is more compact and less active in solution when compared with ΔTM-αVβ3, which lacks the short C-terminal stretches. The structure reveals a bent conformation and defines the α–β interface between IE2 (EGF-like 2) and the thigh domains. Modifying this interface by site-directed mutagenesis leads to robust integrin activation. Fluorescent lifetime imaging microscopy of inactive full-length αVβ3 on live cells yields a donor–membrane acceptor distance, which is consistent with the bent conformation and does not change in the activated integrin. These data are the first direct demonstration of conformational coupling of the integrin leg and head domains, identify the IE2–thigh interface as a critical steric barrier in integrin activation, and suggest that inside-out activation in intact cells may involve conformational changes other than the postulated switch to a genu-linear state.

Introduction

Integrins are α/β heterodimeric type I membrane receptors that mediate divalent cation–dependent interactions with components of the extracellular environment (cells and soluble and matrix proteins) leading to changes in cell shape, movement, growth, differentiation, and survival (Hynes, 2002). Determination of the crystal structure of the ectodomain of αVβ3 (ΔTM-αVβ3) in the absence and presence of a prototypical RGD ligand revealed the modular nature of integrins and clarified the basis of its divalent cation–mediated interaction with extracellular ligands (Xiong et al., 2001, 2002). The 12 extracellular integrin domains are assembled into a head segment mounted on top of two leg segments. The integrin head comprises a seven-bladed β-propeller domain from αV and a vWFA (βA or I-like) domain from β3 and contains the RGD-binding site. The αV leg is composed of an upper Ig-like thigh domain and a lower calf module consisting of two large β-sandwich domains, Calf-1 and -2. The β3 leg consists of an upper leg segment comprising a plexin-semaphorin-integrin (PSI), an Ig-like hybrid, and integrin IE1 (EGF-like 1) domain, followed by a lower leg segment made up of three IE domains (IE2–4) and a novel β-tail domain (βTD). ΔTM-αVβ3 is bent in half at two knee-like joints, the α- and β-genu, the former between the thigh and Calf-2 domains and the latter predicted between IE1 and -2 (Xiong et al., 2001), such that the head and upper leg segments of the heterodimer contact the lower leg segments of the same molecule.

Binding of the F3 subdomain of the talin head to the cytoplasmic tail of the β subunit breaks an α/β salt bridge (that normally stabilizes the inactive state; Wegener et al., 2007), triggering a conformational wave that travels through the α/β transmembrane (TM) and lower leg domains to switch the conformationally sensitive βA domain to a high affinity state, which is a process

Figure 1. Construction, generation, and purification of 1TM-αVβ3. (A) Primary sequence of the exofacial residues and TM domain (underlined) of human αV and β3. The crystal structure of ΔTM-αVβ3 (Xiong et al., 2001) ends at Q956 in αV and G690 in β3 (closed arrows); ΔTM-αIIbβ3 terminates at the corresponding αIIb residue A958 and at G690 in β3 (Zhu et al., 2008). Open arrows point to the C-terminal ends of 1TM-αVβ3 (I967 and V696). G989 in the GFF motif is labeled. (B) Western blot after fractionation on 4–12% gradient SDS gels of LM609 mAb immunoprecipitates from insect cell-free supernatant under nonreducing (NR) and reducing (R) conditions. ΔTM and 1TM indicate ΔTM-αVβ3 and 1TM-αVβ3, respectively. Lanes 1 and 4 show molecular mass (mm) markers. The 1TM-αV and 1TM-β3 subunits migrated with those from ΔTM-αVβ3, as expected for the small (<1%) increase in mass caused by the additional C-terminal sequences. (C) Coomassie-stained purified 1TM-αVβ3 after fractionation on 4–12% gradient SDS gels under nonreducing conditions. Molecular mass markers in lane 1 are indicated.
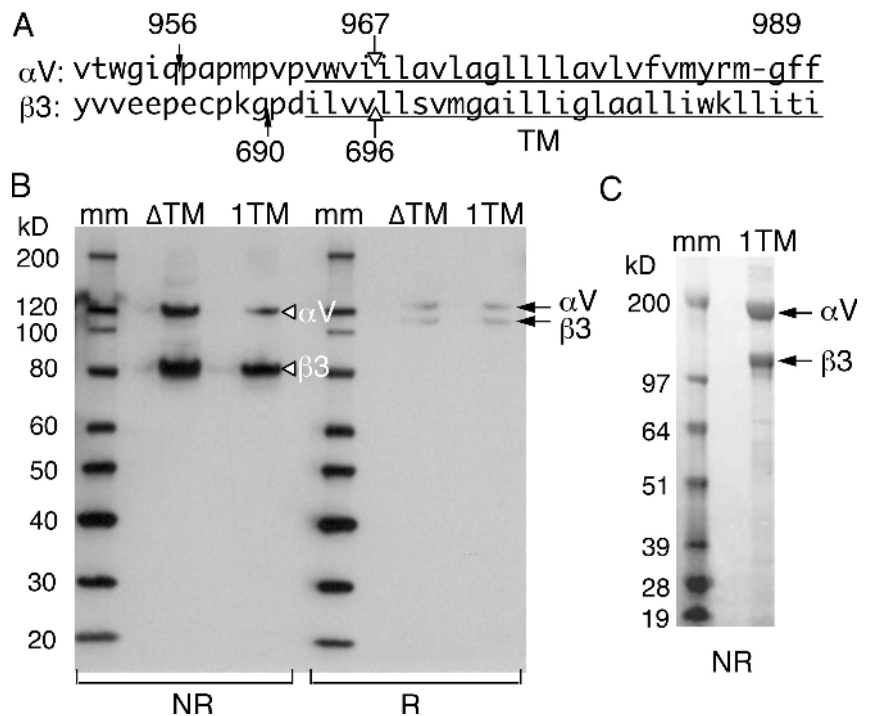
called inside-out activation (Hynes, 2002). Direct evidence for the conformational coupling of the lower leg and head domains is indirect. And how inside-out activation converts the ectodomain to the high affinity state is still ill defined. Modeling the lower integrin legs of the ectodomain perpendicular to the plasma membrane placed the ligand-binding head near the lipid bilayer, seemingly blocking access to macromolecular ligands (for review see Arnaout et al., 2005). A switchblade model (Takagi et al., 2002) proposed that disruption of the α/β cytoplasmic–TM domain interfaces converts the bent ectodomain to a genu-linear conformation, providing ligand access and allowing βA to switch to high affinity. An alternate model, the deadbolt, proposed that lifting the constraints exerted on βA by the lower leg βTD can induce activation without linearity (Xiong et al., 2003). Complete structural information on the remaining α/β residues in the lower leg segments and the conformationally sensitive IE1/IE2 region are missing or incomplete in current structures of the integrin ectodomains (Xiong et al., 2001; Zhu et al., 2008), and knowledge of the distance separating the ligand-binding integrin head from the plasma membrane in the inactive and active states is crucial to elucidate the conformational transitions and energetics of affinity switching in integrins.

In this communication, we engineered a new construct, 1TM-αVβ3, encoding the complete sequence of the αVβ3 ectodomain plus the first four TM residues of each subunit. 1TM-αVβ3 was water soluble at neutral pH and was monomeric, which allowed characterization of its biophysical and functional properties and a determination of its crystal structure. 1TM-αVβ3 was hydrodynamically more compact and less active than ΔTM-αVβ3 in solution. Its crystal structure revealed a bent conformation and defined the complete structure of the ectodomain, including that of the IE1/IE2 region and TM extensions, permitting us to build a structure model comprising the bent ectodomain plus the

complete TM domains (αVβ3-cTM). Functional experiments showed that modifying the defined IE2–thigh interface leads to constitutive activation. Fluorescent lifetime imaging microscopy (FLIM) using ligated Fab fragment of the anti–αV propeller mAb 17E6 (Mitjans et al. 1995) as fluorescence donor and the plasma membrane dye FM4-64 FX as acceptor yielded donor–membrane acceptor separation distances consistent with the αVβ3-cTM structure model, which did not vary between the inactive and active states of the full-length integrin in live cells. These data demonstrate a conformational link between the lower leg and head domains, define the crystal structure of a near native complete ectodomain, identify a critical steric barrier to activation at the IE2–thigh interface, and suggest that the genu-linear state is not an obligate feature of inside-out activation.

Results

Expression and biophysical characterization of 1TM-αVβ3

Published structures of ΔTM-αVβ3 (Xiong et al., 2001) and ΔTM-αIIbβ3 (Zhu et al., 2008) lacked the last seven extracellular residues from the α subunit and P691-D692 from the β3 subunit (Fig. 1 A). We expressed in insect cells an αVβ3 ectodomain, 1TM-αVβ3, encoding all of the missing extracellular residues in addition to a four-residue TM extension of each subunit. 1TM-αVβ3 was secreted into the culture supernatant of virus-infected High-Five insect cells (Fig. 1 B) and was purified by affinity chromatography (Fig. 1 C).

The isocratic elution profiles of purified 1TM-αVβ3 and ΔTM-αVβ3 were compared on molecular sieve chromatography columns in neutral buffer containing the physiological divalent cations 1 mM Ca^{2+} + 1 mM Mg^{2+} (Ca^{2+}/Mg^{2+}) or 1 mM of the activating cation Mn^2. The apparent hydrodynamic radius (Stokes
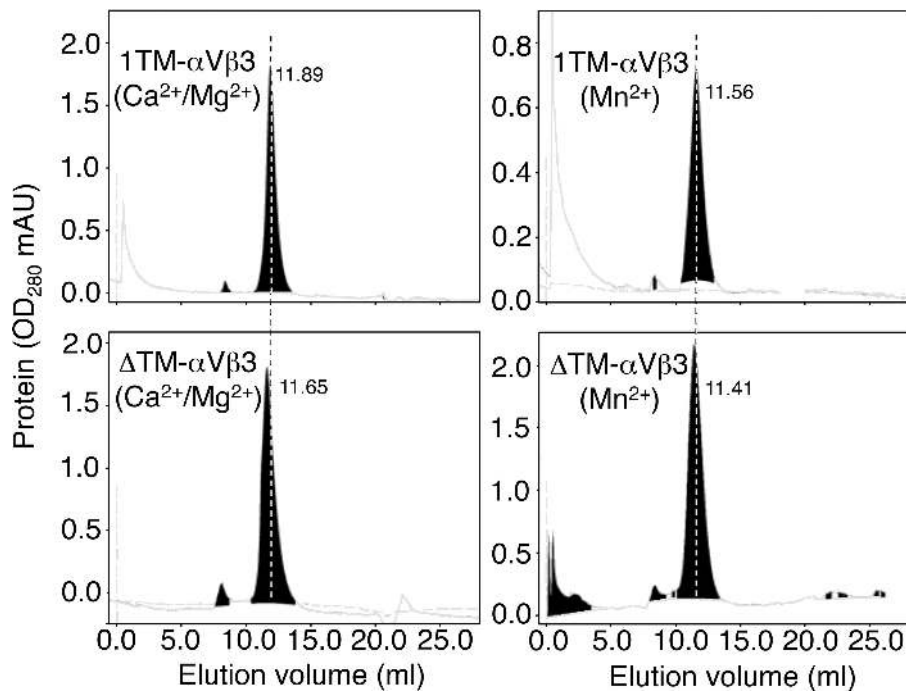
Figure 2. **Hydrodynamic analyses of 1TM-αVβ3 and ΔTM-αVβ3 by molecular sieve chromatography.** A representative experiment (one of four) is shown. Purified ΔTM-αVβ3 or 1TM-αVβ3 in TBS, pH 7.4, containing 1 mM MgCl₂ + 1 mM CaCl₂ or 0.2 mM MnCl₂ was analyzed. Each integrin was applied onto a precalibrated Superdex S-200 GL column, and Stokes radii were derived as described previously (Adair et al., 2005). Values next to the major peaks indicate peak elution volumes (in milliliters). A dashed line was added to emphasize the peak shifts. mAU, milli–absorbance unit.

radius [Rs]) of 1TM-αVβ3 was calculated by reference to the elution position of standard proteins (Fig. 2). Rs of 1TM-αVβ3 changed from 55 ± 0.41 Å (mean ± SD; $n = 4$) in Ca²⁺/Mg²⁺ to 58 ± 0.3 Å in Mn²⁺. The Rs values for ΔTM-αVβ3 in Ca²⁺/Mg²⁺ and Mn²⁺ were 57 ± 1.1 Å and 60 ± 1.1 Å, respectively. Thus, the mean Rs value for 1TM-αVβ3 in Mn²⁺ differed little from that of ΔTM-αVβ3 in Ca²⁺/Mg²⁺. The small amounts of oligomers in the ΔTM-αVβ3 preparations in the presence of Mn²⁺ were largely absent in 1TM-αVβ3, and the peak width at half height, which is a measure of molecular heterogeneity, was narrower for 1TM than for ΔTM. These data suggest that the short C-terminal α/β extensions introduced in 1TM result in a more compact and homogenous molecule in solution.

Binding of soluble 1TM-αVβ3 to physiological ligands and to the activation-sensitive mAb AP5

We performed dose–response curves to quantify the binding of increasing concentrations of 1TM-αVβ3 to immobilized FN7–10 in Mn²⁺ and in Ca²⁺/Mg²⁺ (Fig. 3, A and B). Half-maximal binding was achieved at 0.1 μg/ml and 6.0 μg/ml, respectively ($n = 2$). For soluble ΔTM-αVβ3, half-maximal binding was achieved at 0.15 μg/ml and 1.6 μg/ml, respectively. No binding took place to uncoated wells or fibronectin (FN)-coated wells in the presence of cilengitide (unpublished data). Soluble 1TM-αVβ3 formed a stable complex with either FN7–10 (Fig. 3 C) or native full-length FN (Fig. 3 D and Table S1) in solution in Mn²⁺-containing buffer (Fig. 3 D and Table S1). Also consistent with the solid phase binding assays, soluble 1TM-αVβ3 did not form a stable complex with either FN7–10 or full-length FN in Ca²⁺/Mg²⁺ buffer (Fig. 3 D, inset; Table S1; and not depicted). However, soluble 1TM-αVβ3 formed a stable complex in 2 mM of CaCl₂ (or Ca²⁺/Mg²⁺) buffer with the Fab fragment of AP5 (Fig. 3 E), a ligand-inducible binding site mAb which binds

αVβ3 in its active or RGD-bound states but not in its inactive state (Honda et al., 1995; Faccio et al., 2002).

Crystal structure of 1TM-αVβ3

A new native dataset derived from one 1TM-αVβ3 crystal let us determine the structure of the 1TM-αVβ3, including the TM extensions, at 2.9-Å resolution (Fig. 4). The structure was superposable on the ΔTM-αVβ3 structure (Xiong et al., 2001, 2004) except for those regions newly expressed, the C-terminal exofacial, and the TM residues (Fig. 4 A) and now resolved the IE1 and -2 domains (Fig. 4, B–D). The nearly parallel exofacial extensions I955-P959 (in αV) and P688-G690 (in β3) remain close through A958 and G690 (Cα–Cα = 6.2 Å) and then diverge at an extended Pro-rich loop structure in αV (P959APMPVP963) before the first putative α TM residue V964. Structure search of this Pro-rich sequence yielded such loops in two contexts (Protein Data Bank numbers 2w55 and 2q0s), suggesting that this extended structure is not a crystal artifact but also exists in the native integrin. The first TM residues V964 (in αV) and I963 (in β3) occupy similar positions in the structure, but the TM extensions do not assume the α-helical turns found in the nuclear magnetic resonance (NMR) structure of the α/β TM domains (Lau et al., 2009) and do not interact as the result of unfavorable crystal contacts.

The three tandem integrin domains IE2–4 are related by an approximately twofold screw axis symmetry and form an extended module (Fig. 4 C). IE1 is roughly antiparallel to IE2, as a result of the bend at the β-genu (Fig. 4 C). Each IE domain has three disulphides (a–c) having the same connectivity a$_N$-a$_C$, b$_N$-b$_C$, c$_N$-c$_C$ as that found in other EGF domains (Fig. 4 E; Wouters et al., 2005). IE1 lacks disulphide a (a$_N$-a$_C$), thus potentially avoiding a clash with the adjacent PSI domain. A characteristic forth N-terminal intradomain disulphide d (d$_N$-d$_C$) occupies an analogous site to the Ca coordination site found in the Ca-binding subset of EGF domains (Wouters et al., 2005). IE1–4 each contain
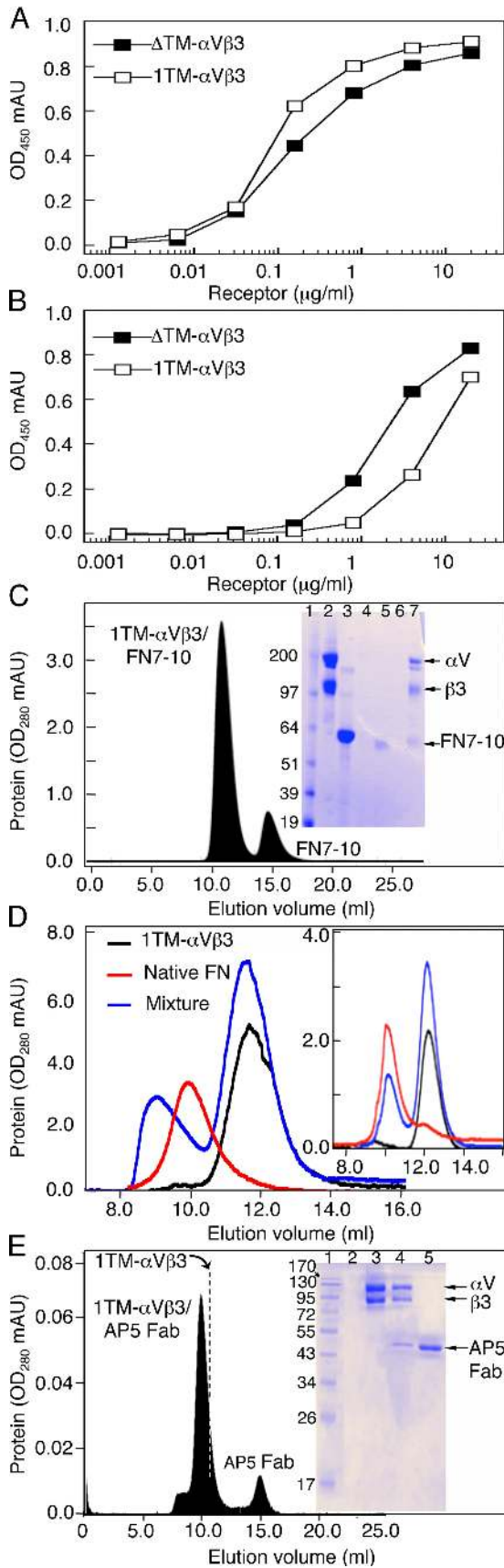
three β strands (A–C), with the first two antiparallel strands (A and B) forming a major β sheet found in classical EGF domains. Strand C is hydrogen bonded to strand D, which is contributed in part by the consecutive domain, with strands C and D forming a minor β sheet–like conformation. A short strand D caps the IE4 domain, which is stabilized by the C601-C604 disulphide linker that precedes the start of the βTD. In IE1–4, strand D has a characteristic β bulge at a conserved E/N residue (E472, E522, N559 and E599, respectively) to allow accommodation of disulphide c; its cross-strand partner in strand C is an invariant Gly (G468, G518, G555, G595, respectively), which is found typically in class II EGF domains (Wouters et al., 2005) and some laminin-type epidermal growth factor–like domains (Stetefeld et al., 1996).

IE2 has two characteristically long loops, c (between c_N and c_C) and d (between d_N and a_N; Fig. 4 E), with the latter housing the β-genu (Fig. 4 B). The β-genu is clearly visible in the electron density map despite lack of crystal contacts from symmetry-related molecules, which is stabilized by hydrogen bonds to the major sheet of IE2. The two long loops and strand A of IE2 face the bottom of the thigh domain, making mainly electrostatic contacts with its CC′ and EF loops (Fig. 4 D). The minor strand of IE2 faces the N-terminal segment of PSI and forms ionic and van der Waals contacts involving mainly T7-R8 of the PSI domain.

Extending the 1TM structure into the α/β TM fragment, which overlaps with structured residues in the NMR structure of αIIbβ3 TM domains (Lau et al., 2009), allowed us to build a structure model of the inactive ectodomain plus the complete TM domains (Fig. 4, F–H). In this model, the ligand-binding site is accessible to macromolecular ligands, and the extracellular membrane proximal segment is structured. By comparison, in the recent structure model of the αIIbβ3

Figure 3. **Binding of 1TM-αVβ3 to physiological ligands and to the Fab fragment of the activation-sensitive mAb AP5.** (A and B) Receptor-binding assay to immobilized ligand. Dose–response curves showing
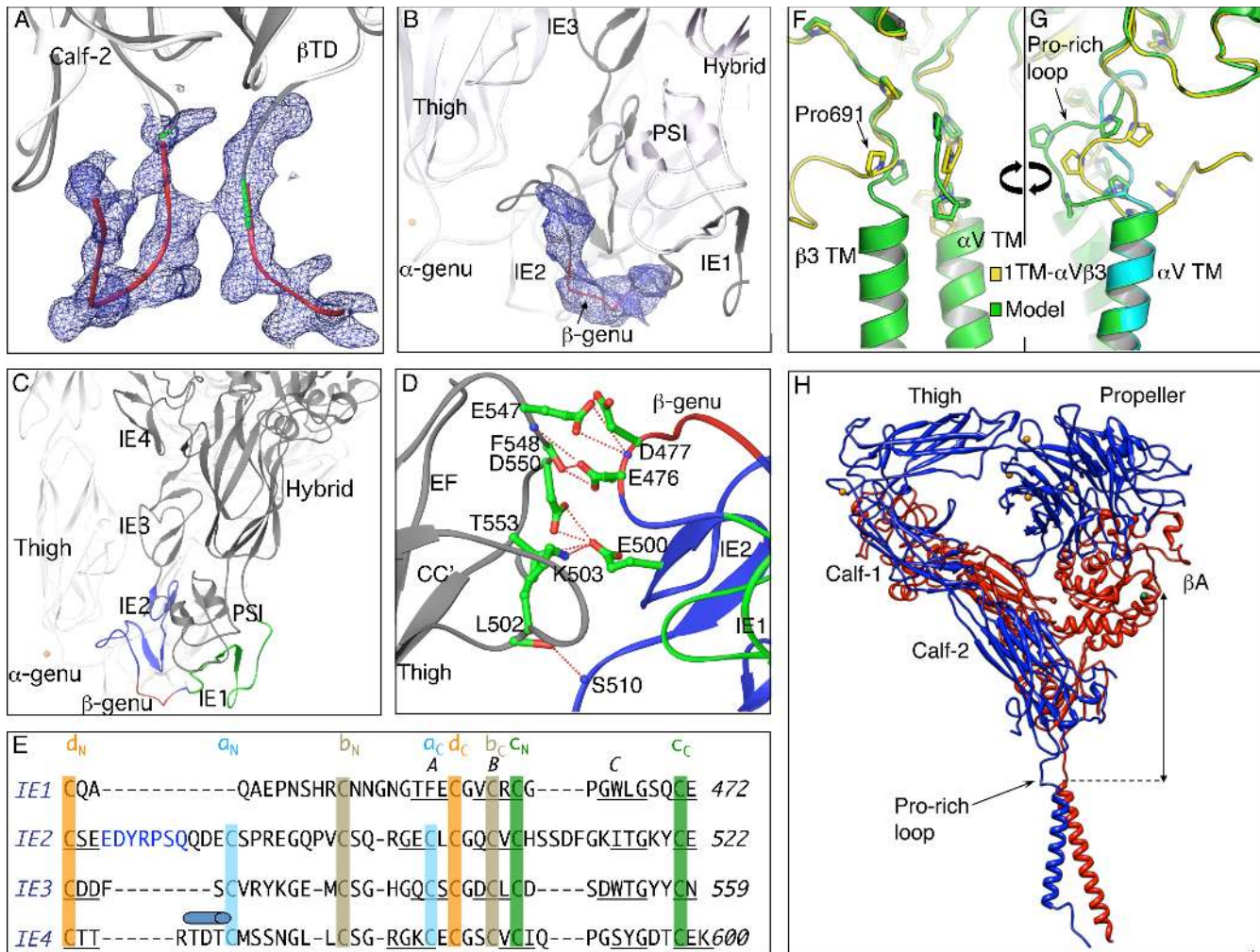
Figure 4. **New features of 1TM-αVβ3 crystal structure and hypothetical model of αVβ3 plus the complete TM domains (αVβ3-cTM).** (A) Density map (in blue; contoured at 1.0 σ) of the exofacial and TM extensions. The superposed main chains of 1TM-αVβ3 and ΔTM-αVβ3 (only the lower parts of Calf-2 and βTD shown from each; Xiong et al., 2004) are in light and dark gray, respectively, except for the new exofacial and TM extensions of 1TM-αVβ3, which are shown in red, and the last residues in the ΔTM-αVβ3 structure (Q956 and G690), which are shown in green. (B) Density map (in blue; contoured at 1.0 σ) and main chain tracing of the β-genu (in red) in IE2. The orange sphere in this panel and in C represents the metal ion at the α-genu. (C) Ribbon diagram of the IE1–IE2 region in a similar orientation to that shown in B. Main chain tracings of IE1, IE2, and β-genu are in green, blue, and red, respectively. (D) Ribbon diagram showing electrostatic interactions at the IE2–thigh interface. Residues (shown in ball and stick representation) forming a salt bridge, main chain, or side chain H-bonds are labeled. Thigh and IE2 are labeled in gray and blue, respectively, with the β-genu in IE2 shown in red. Oxygen, nitrogen, and carbon atoms are in red, blue and green, respectively. Hydrogen bonds and salt bridges (distance cutoff, 3.5 Å) are represented with red dotted lines. (E) Structure alignment and Cys pairing of IE domains. The sequence housing the β-genu in IE2 is in blue. The secondary structure elements (strands are underlined, and a helix is represented by a cylinder) are shown. The atomic coordinates are deposited in the Protein Data Bank (3IJE). (F–H) Structure model of αVβ3 ectodomain plus the complete TM domains (αVβ3-cTM). The model is built by releasing the C termini in the 1TM-αVβ3 structure from their respective crystal contacts, such that extracellular P691 and P963 initiate the respective β3 and αV TM helices, which is consistent with the known propensity of prolines to strongly stabilize α-helical conformations (Senes et al., 2004). (F and G) The resulting movements included a 2.9-Å inward movement of P691 of β3 (F) and a rotation of αV's Pro-rich loop at Q956, such that P963 initiates the αV TM helix (modeled after αIIb's TM NMR structure; G; Lau et al., 2009). The structure model was energy minimized with Modeller (Fiser and Sali, 2003), and the αVβ3 TM side chains were optimized and repacked using Rosetta (Rohl et al., 2004). The ribbon diagrams in F and G were generated using PyMOL (DeLano Scientific LLC). (H) A ribbon diagram, which was generated using Chimera, of the αVβ3-cTM model showing the orientation of the ectodomain relative to the TM domains. The model predicts that the TM domains are at an ∼30° angle relative to the long axis of Calf-2, with ADMIDAS (adjacent to MIDAS) metal ion (green sphere) at an ∼45-Å distance from the plane parallel to the hypothetical membrane drawn at the Cα of β3's Pro691. The α-genu and propeller metal ions are in orange.

ectodomain plus TM domains (Zhu et al., 2009), this region is not structurally defined and assumed to be very flexible in the inactive integrin model. However, inserting a flexible linker into the extracellular membrane proximal Pro-rich sequence of the β2 integrin α subunit CD11b leads to a constitutively active integrin (Kamata et al., 2005), suggesting that some rigidity in this region is essential to maintain the integrin in its inactive conformation.

Functional effects on activity of full-length αVβ3 after mutation of features structurally defined in the 1TM structure

We assessed the effects on cellular αVβ3 caused by modifying the newly defined IE2–thigh interface through a Δβ-genu deletion (Δβ-genu), altering the βTD–hybrid–IE3 interfaces by breaking two salt bridges (R404A + R633A), and changing the βA–βTD–hybrid interfaces by deleting the βTD CD loop plus

Figure 5. **Effect of mutations based on the TM-αVβ3 structure on integrin activation.** The histogram (mean ± SD; $n = 3$) shows binding of Alexa Fluor 488–FN9–10 to WT and mutant surface-expressed αVβ3. The percentage of FN9–10-bound cells was expressed as a percentage of AP3-bound cells. Binding of WT and each of the mutants in Ca^{2+}/Mg^{2+} was then expressed as a percentage of that obtained for the Mn^{2+}-activated WT integrin, with the latter set at 100.
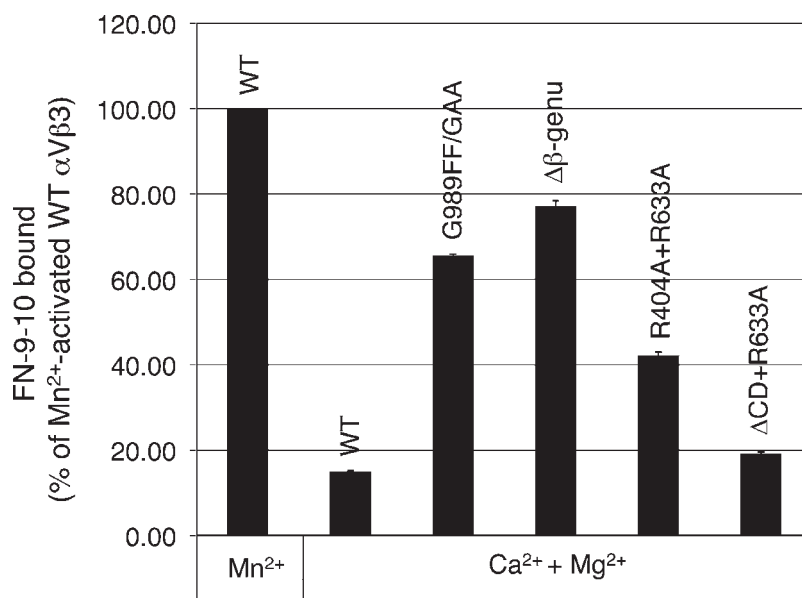
an R633A substitution (ΔCD + R633A). The activating G989FF/GAA mutation (Zhu et al., 2007) served as a positive control. None of the mutations impaired expression or heterodimer formation compared with wild type (WT), as judged by reactivity with the β3-specific AP3 mAb and the heterodimer-specific LM609 mAb (unpublished data). Mn^{2+} increased binding of the WT receptor to soluble Alexa Fluor 488–labeled FN9–10 from 7% in Ca^{2+}/Mg^{2+} buffer to 48% of the AP3-positive cell population in Mn^{2+}. The Δβ-genu mutation induced constitutive activation that was significantly more robust than the G989FF/GAA mutant (Fig. 5), with a more modest activation induced by the R404A + R633A mutation. The activating effect of the ΔCD + R633A mutation was small but significant (P < 0.005; Fig. 5).

FLIM analysis of αVβ3 in live cells

We used FLIM to assess the orientation of the αVβ3 ectodomain relative to the plasma membrane in K562 cells stably expressing WT αVβ3. For lifetime calculations, FLIM collects only photons emitted from the donor fluorophores, thus avoiding the problem of mis-excitation of the acceptor and the analogous problem of spectral break through bleeding of the donor signal into the acceptor spectral window, which are common concerns in spectral fluorescence resonance energy transfer (FRET) applications (Chigaev et al., 2001; Kim et al., 2003; Coutinho et al., 2007). Importantly, FLIM allows picosecond measurements and is independent of concentration of the fluorophores.

As fluorescence energy transfer between a donor–acceptor pair described by the Förster equation depends both on the distance and the relative orientation of donor and acceptor (Jares-Erijman and Jovin, 2003; Giepmans et al., 2006), it is critical that a structurally defined probe be used as donor. Therefore, we used the Fab fragment of mAb 17E6 whose low resolution epitope mapping (Mould et al., 2000) corresponds to its crystal structure bound to the β-propeller of ΔTM-αVβ3, which we have determined (17E6 binds at the top of the propeller contacting the DA loop between blades 2 and 3 and the CD loop in blade 3; unpublished data). Binding of unlabeled 17E6 Fab to the cell surface

Mn^{2+}-activated WT αVβ3 did not affect binding of fluorescently labeled soluble monomeric FN10, either as WT or as a high affinity form (Fig. 6 A). The RGD ligand cilengitide also triggered an increase in hydrodynamic radius of the 17E6–1TM-αVβ3 complex (Fig. 6 B), indicating that 17E6 Fab did not freeze either membrane-bound or soluble αVβ3 in an inactive state. The plasma membrane was labeled with FM4-64 FX (FM) as acceptor. This dye preferentially inserts into the outer leaflet of the membrane of live cells in 1–5 min at 4°C, fluoresces brightly, and can be rapidly fixed with ice-cold paraformaldehyde, eliminating diffusion on the time scale of FLIM measurements. The standard equation to calculate FRET efficiency applies to populations of fluorophores in such circumstances and is frequently used in biological systems to report mean donor–acceptor distances.

Alexa Fluor 488 fluorescence lifetime was first measured in inactive WT αVβ3–expressing K562 cells stained with Alexa Fluor 488–Fab in 1 mM of $CaCl_2$-containing buffer. A lifetime of 2,306 ± 52 ps (mean ± SD) was determined in the absence of acceptor (Fig. 6, C and D). When the Alexa Fluor 488–Fab-labeled K562 cells were further labeled with the FM membrane dye, Alexa Fluor 488 lifetime decreased to 2,056 ± 118 ps (P < 0.0001), corresponding to a FRET efficiency of 10.8% and a mean donor–acceptor separation distance (r) of 88 Å. The respective values for the Mn^{2+}-activated αVβ3 were 2,322 ± 43 ps in the absence of acceptor and 2,087 ± 118 ps (P < 0.0001) after addition of the FM dye, corresponding to a FRET efficiency of 10.1% and a mean donor–acceptor separation distance (r) of 89 Å. This distance is consistent with the hypothetical structure model depicted in Fig. 4 H, which predicts an ∼90-Å distance from the centroid of the integrin-bound 17E6 Fab to the plane of the membrane parallel drawn at the Cα of β3's P691 residue. Mean donor–acceptor separation distances of 78 ± 9 Å (mean ± SD) and 83 ± 3 Å were obtained with unliganded αVβ3 and with high affinity FN10-bound αVβ3, respectively, each in 1 mM of Mn^{2+}-containing buffer. FLIM measurements conducted on transiently transfected HEK 293T cells expressing WT, G989FF/GAA, or Δβ-genu αVβ3 in 1 mM of Mn^{2+}-containing buffer
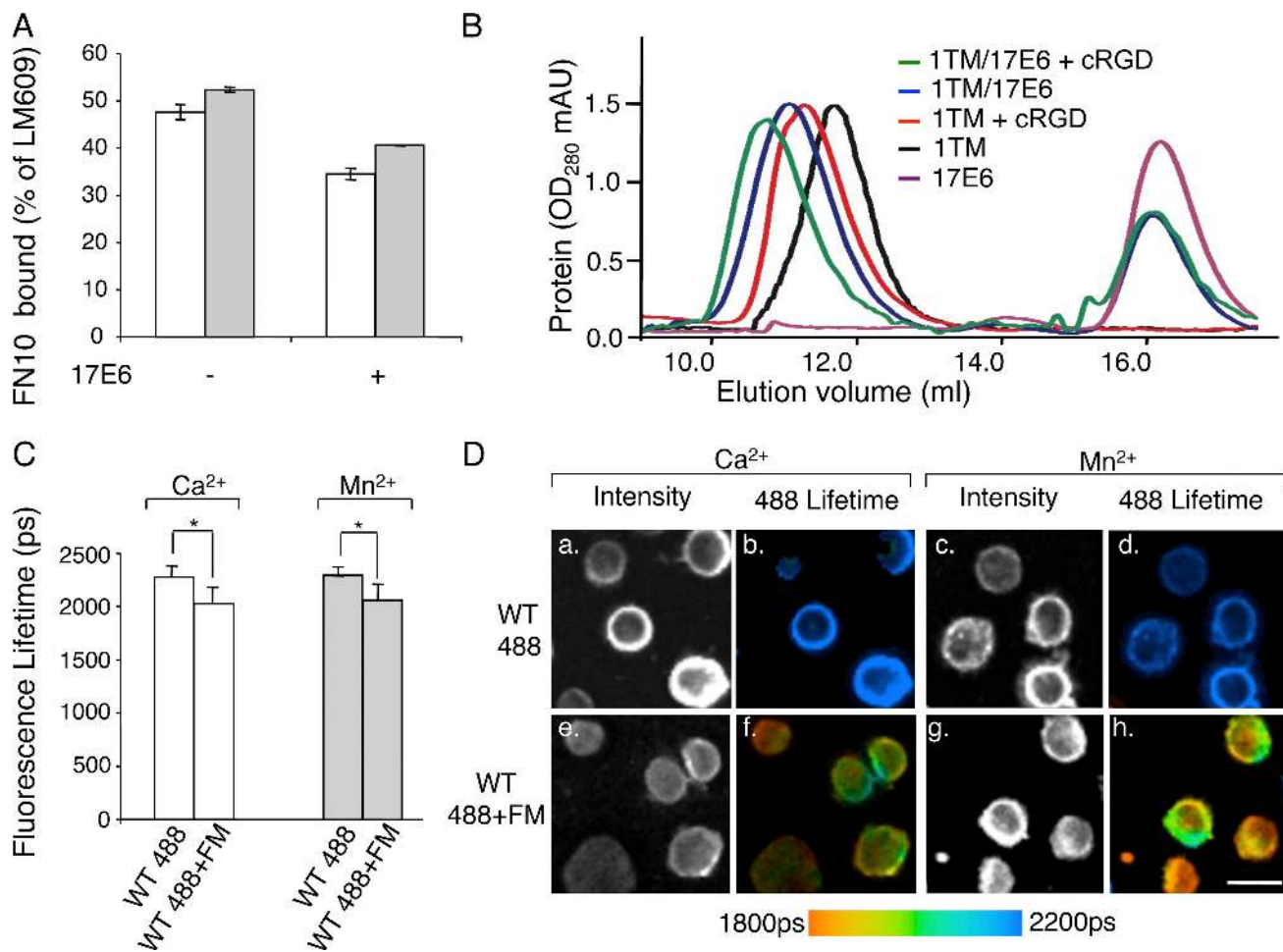
Figure 6. **FLIM analysis of αVβ3 in live cells.** (A) Histogram (mean ± SEM; $n = 2$) showing binding of subsaturating Alexa Fluor 488–labeled WT (open bars) and high affinity (h; shaded bars) FN10 to full-length WT αVβ3 stably expressed on K562 in the absence (−) or presence (+) of saturating amounts of unlabeled 17E6 Fab in 1 mM Mn^{2+} (see Materials and methods). (B) Isocratic molecular sieve elution profiles in Mn^{2+}-containing TBS buffer. 1TM-αVβ3 (black) and its complexes with cilengitide (red), 17E6 Fab (blue), and 17E6 Fab complex followed by the addition of cilengitide to 10 μM (green) were resolved. The elution profile of 17E6 Fab alone is also shown (violet). Cilengitide runs in the column volume. Cilengitide triggers an increase of the apparent Stokes radius of the 1TM-αVβ3–17E6 Fab complex. mAU, milli–absorbance unit. (C) Histogram (mean ± SD) showing lifetimes (in picoseconds) of Alexa Fluor 488 fluorescence determined by FLIM in inactive (Ca^{2+}) and active (Mn^{2+}) full-length αVβ3. *, $P < 0.0001$ versus donor only. (D) Representative Alexa Fluor 488 fluorescence intensity of the unliganded WT integrin. The pseudocolored FLIM images represent donor fluorescence lifetimes on a pixel by pixel basis, where shorter lifetimes are located toward the red area of the spectrum and longer lifetimes toward the blue area. Bar, 8 μm.

yielded mean donor–acceptor separation distances of 96 Å, 94 Å, and 90 Å, respectively. Thus, the donor–acceptor separation distances are comparable in the inactive, Mn^{2+}-activated, constitutively active, or FN10-bound states of the full-length αVβ3 expressed on the surface of live cells. It is appropriate to mention here that the calculated length of the genu-linear αVβ3 molecule is >200 Å (Xiong et al., 2001).

Discussion

Our major findings in this study are that (a) the C-terminal extensions of the αVβ3 ectodomain by the remaining exofacial residues and four α/β TM residues gave a water soluble and conformationally stable integrin that is predominantly inactive in Ca^{2+}/Mg^{2+} buffer in solution, (b) crystal structure of the near native 1TM-αVβ3 in Ca^{2+} defined the first complete structure of an integrin ectodomain plus an α/β TM fragment and allowed us to build a structure model of the ectodomain plus the complete

TM domains, (c) functional analyses using the 1TM-αVβ3 crystal structure identified a critical role for the newly defined IE2–thigh interface in integrin activation, and (d) FLIM of WT αVβ3 in live cells revealed that the apparent distance between the integrin head and the plasma membrane changes little in inactive, Mn^{2+}-activated, constitutively active, or FN10-bound full-length integrin.

We found that 1TM-αVβ3 is recognized in solution by the activation-sensitive mAb AP5 in 2 mM Ca^{2+} but did not form a stable complex in solution with FN7–10 or full-length FN, unless the integrin is activated by Mn^{2+}. Quantitative binding assays showed that $K_{d(app)}$ values of 1TM-αVβ3 and ΔTM-αVβ3 binding to immobilized FN7–10 in Mn^{2+} are comparable (0.15 and 0.1 μg/ml). However, binding of 1TM-αVβ3 and ΔTM-αVβ3 in Ca^{2+}/Mg^{2+} buffer yielded $K_{d(app)}$ values that were ∼60-fold and ∼10-fold lower, respectively, than in Mn^{2+} (Fig. 3, A and B), reflecting the proportion of the active species in each preparation. Thus, 1TM, which differs only in the added α/β lower leg, is less active and

hydrodynamically more compact than ΔT, reflecting a conformational coupling between the lower leg and head domains that regulates integrin activation. Our present findings are also consistent with the integrin existing in equilibrium between two major quaternary states, inactive (T state) and active (R state; Perutz, 1989), with the T state predominating in soluble 1TM-αVβ3 in Ca^{2+}/Mg^{2+} buffer. mAb AP5 binds preferentially in Ca^{2+} or Ca^{2+}/Mg^{2+} buffer to the minor active species (estimated at ∼2% and ∼10% in 1TM- and ΔTM-αVβ3 preparations, respectively), driving the quaternary equilibrium toward the active quaternary state (s) and stabilizing it there (Fig. 3 E). The same shift can be accomplished by FN7–10 or by native FN but requires Mn^{2+} not Ca^{2+}, presumably because of the higher affinity of Mn^{2+} to the metal ion–dependent adhesion site (MIDAS) that mediates αVβ3 interaction with ligands. Using the measured $K_{d(app)}$ values as approximations of binding affinities, the mean difference in energy between the two major quaternary states of 1TM- and ΔTM-αVβ3 is estimated at ∼2.4 kcal/mol and 1.4 kcal/mol, respectively. It is expected that this value will be even higher for the full-length integrin.

The crystal structure of ΔTM-αIIbβ3 at 2.55-Å resolution reported (Zhu et al., 2008) while this work was under review ends at the equivalent residues to ΔTM-αVβ3 and thus lacks those lower leg residues and TM fragments defined in the current 1TM-αVβ3 structure and shown to regulate affinity. Superposition of the ΔTM-αIIbβ3 structure onto that of 1TM-αVβ3 using Matchmaker in the Chimera software suite (Pettersen et al., 2004) revealed several interesting differences between these two structures. First, a significant inward rotation of Calf-1 and -2 at the α-genu in ΔTM-αIIbβ3 resulting from crystal contacts with symmetry-related molecules was associated with translational movements in the IE2–4 domains. Second, the β-genu is missing in the ΔTM-αIIbβ3 structure, where it is presumed disordered (Zhu et al., 2008). Yet, significant changes appear in the main chain flanking the β-genu in ΔTM-αIIbβ3 compared with 1TM-αVβ3, suggesting proteolytic cleavage within this site in ΔTM-αIIbβ3 as another likely explanation. Third, the βTD of ΔTM-αIIbβ3 veers toward IE4 and away from the hybrid/βA domains, breaking the R633-coordinated salt bridge, which stabilizes the inactive state of full-length αIIbβ3 (Matsumoto et al., 2008). The engineered disulphide linking βTD to Calf-2 in ΔTM-αIIbβ3 may impose these quaternary changes in the βTD environment. Fourth, the βA domain of unliganded ΔTM-αIIbβ3 contained the MIDAS and the stimulatory ligand-associated metal-binding site (LIMBS) metal ions (Mg^{2+} and Ca^{2+}, respectively), but no metal ions were present in the 1TM-αVβ3 2.9-Å structure formed in the presence of Ca^{2+} (Fig. S1) or in our published 3.1-Å unliganded ΔTM-αVβ3 structure (Xiong et al., 2001), even when Mn^{2+} was diffused into the crystals. Lower resolution (Zhu et al., 2008) is an unlikely explanation for this difference, as both metal ions are overt in the 3.2-Å structure of the ΔTM-αVβ3–cRGD complex (Xiong et al., 2002). Furthermore, in native βA isolated from the β3 subunit, LIMBS did not bind Ca^{2+} (Pesho et al., 2006), so the absence of a LIMBS Ca^{2+} in unliganded β3 is independently supported. Whether clasping the legs covalently by an artificial disulphide permits metal occupancy at LIMBS through allosteric mechanisms remains an open question. A likely interpretation is that the difference reflects an influence of the associated α subunit

on the metal ion coordination in βA. In the unliganded ΔTM-αIIbβ3 structure, the LIMBS residue D^{217} points toward LIMBS (and not away from it as in 1TM-αVβ3) to avoid a clash with a hydrophobic residue (Phe191, which is a Trp in all other α subunits; Fig. S1). This orientation provides five coordination sites for a LIMBS Ca^{2+}, with the sixth coordination site completed by OE1 of E220, which is thus pulled out of the MIDAS pocket, allowing coordination of an Mg^{2+} at the MIDAS.

As 1TM-αVβ3 is the fourth integrin crystal structure resolved in a bent conformation under conditions that activate ligand binding in biochemical and cell biological assays, we once again addressed the contentious issue of the conformation of the integrin αVβ3 at the cell surface. We positioned a FLIM donor on the integrin head and an acceptor in the outer face of the plasma membrane. FLIM measurements revealed no significant change in mean separation distance of the integrin head relative to the plasma membrane outer face in Mn^{2+}-activated WT αVβ3 compared with the inactive integrin (Fig. 6, C and D). A previous FRET study measured the distance between an FITC-labeled ligand-mimetic peptide as donor and a plasma membrane dye as acceptor (Chigaev et al., 2003). There, the change in mean distance of closest approach was ∼50 Å between resting and Mn^{2+}-activated α4β1. However, as stated by the authors, the membrane dye used, R18, has a tendency to flip-flop between the outer and inner leaflets of the plasma membrane, introducing uncertainty in the measurements. The FLIM methodology we have used minimizes this problem and supports a more recent cryoelectron tomography study of liposome-embedded and Mn^{2+}-activated αIIbβ3 (Ye et al., 2008). Interestingly, high affinity soluble monomeric FN10 bound to the WT αVβ3 in Mn^{2+} or the constitutive activation of αVβ3 by G989FF/GAA or Δβ-genu mutants also failed to trigger an increase in the mean donor–membrane acceptor separation distance compared with the inactive WT integrin. The simplest explanation for these data is that a switch of the integrin from the inactive to the active state or its binding to soluble FN10 in live cells can occur with little or no genu extension, which is consistent with a recent modeling study (Rocco et al., 2008).

The functional experiments presented in this study identify a previously unappreciated but critical role for the IE2–thigh interface in stabilizing the inactive state (Fig. 7). This is reflected by the robust constitutive activation introduced in the surface-expressed receptor upon deletion of the β-genu, which contributes to this interface. Our results also show that stability of the IE2–thigh interface appears to be conformationally linked to the lower leg extensions introduced in 1TM-αVβ3. Other mutations in the lower leg domain that interrupt two salt bridges linking the βTD and IE3 to the top and bottom of the hybrid domain, respectively (Fig. 7), revealed that these make a modest contribution to stability of the inactive state: in αVβ3, the steric barrier is mainly mediated by the IE3–hybrid contact, whereas the βTD–hybrid contact appears to predominate in αIIbβ3 (Matsumoto et al., 2008). Our functional experiments also show that βTD contacts with both βA and hybrid domains contribute to stability of the inactive conformation, although this contribution is minor in αVβ3 and absent in αIIbβ3 when the βTD–βA contact alone is removed by deleting the CD loop in βTD (Zhu et al., 2007).
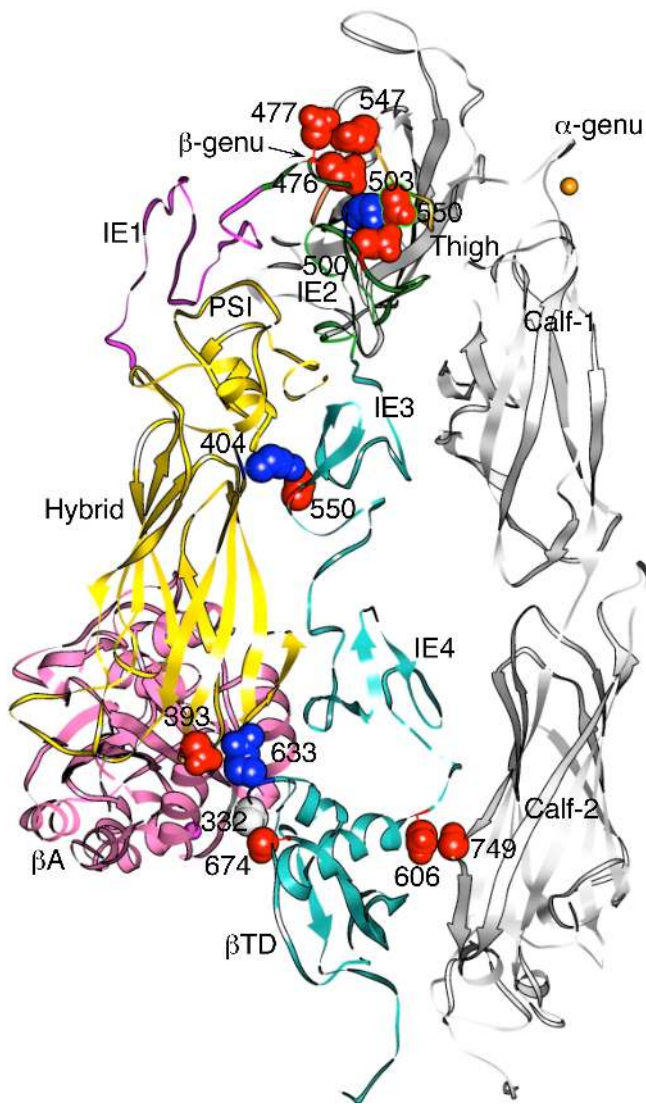
Figure 7. **Ribbon diagram showing functionally relevant ionic contacts in the 1TM-αVβ3 structure.** IE2 makes several electrostatic contacts with two conserved loops at the bottom of the thigh domain. These include E500 from IE2 making a salt bridge with the conserved CC′ loop residue K503 and an H-bond with the invariant EF loop residue D550 (both from the thigh domain) and the β-genu residues E476 and D477 making H-bonds with the EF residue E547. Two salt bridges (R633–D393 and R404–D550) link the top and bottom of the hybrid domain to βTD and IE3, respectively. The small βTD–βA interface (S674–V332, in gray) and an H-bond between the βTD (D606) and Calf-2 (S749; Kamata et al., 2005) are also shown.

Previous studies have shown that disulphides introduced at the βTD–βA or βTD–Calf-2 interfaces blocked integrin activation (Takagi et al., 2002; Kamata et al., 2005), suggesting that the small barriers at these nodes must also be overcome in the conformational switch of the integrin to the active state. Collectively, these data suggest that binding of the F3 subdomain of talin to the β3 cytoplasmic tail (mimicked by the G989FF/GAA mutant; Wegener et al., 2007) unravels the α/β TM packing, triggering movement of the membrane-proximal lower leg domains, reducing the energy cost of destabilizing the critical IE2–thigh interface (Fig. 7), which then drives the conformational equilibrium toward the quaternary R state almost completely (Fig. 5).

The shape of the quaternary R (active) state of the integrin ectodomain remains to be defined structurally. But it includes the high affinity state of βA and a proposed genu-linear conformation, which, it is argued, is required for switching βA to the active state (Takagi et al., 2002). In the homologous αA domain, the high affinity state is characterized by an inward movement of the N-terminal α1 helix and a two-turn downward movement of the C-terminal α7 helix, which is permitted by a flexible long linker distally (Lee et al., 1995). The former movement was observed in the crystal structure of the bent cRGD-bound ΔTM-αVβ3 (Xiong et al., 2002) but in the absence of the axial movement of α7 helix, which is constrained distally in the bent crystal structure by the hybrid domain. The activating effect of releasing constraints on the hybrid in the R633 + R404 mutant is consistent with previous work performed on integrin ectodomains with modified, truncated, or entirely amputated legs (Mould et al., 2003; Xiao et al., 2004), which found a correlation between opening the βA–hybrid hinge and the high affinity state of βA. An ∼70° hinge opening in the legless ectodomain structure (Xiao et al., 2004), which is associated with a one-turn downward movement of the C-terminal α7 helix, led to the conclusion that this feature characterizes the high affinity state of βA. However, a recent study (Chigaev et al., 2009) found that the hybrid domain movement and the high affinity state are regulated separately and independently of each other. And an EM study of the intact ΔTM-αVβ3 ectodomain complexed with FN7–extra do-main B–10 detected only a small 11 ± 4° opening of the βA–hybrid hinge angle (Adair et al., 2005), which is sufficient to break the IE2–thigh interface, suggesting that a rather modest hinge opening may be all that is needed to switch βA to high affinity. Consistently, a molecular dynamics study of the legless αIIbβ3 ectodomain detected a spontaneous βA–hybrid hinge opening of ∼20° when a single N303-K417 bond linking βA to hybrid is broken (Puklin-Faucher et al., 2006), but over the course of this increase, a lateral rather than the axial shift of the βA domain C-terminal α7 helix was observed. The same study found that subsequent pulling on bound FN10 caused the βA–hybrid domain hinge to further increase to 70° in the legless ectodomain, suggesting that the wider hinge opening requires force applied on a ligand-bound integrin. Whether such an extreme movement requires preconversion of the ectodomain to a genu-linear structure or can occur in a genu-bent conformation requires further study. Our data suggest that overcoming the critical IE2–thigh steric barrier through the activating β-genu deletion does not require a genu-linear conversion. It may also be relevant that binding of soluble monomeric high affinity FN10 did not induce genu linearity in the full-length αVβ3, suggesting that the high affinity state and genu linearity are not conformationally linked events, an interpretation which is consistent with experimental observations in WT and modified integrins (Takagi et al., 2003; Coutinho et al., 2007; Gupta et al., 2007). It has been proposed that genu linearity requires force applied by the cytoskeleton to the cytoplasmic tails of the unliganded integrin (Zhu et al., 2008). However, our FLIM data on constitutively active αVβ3 suggest that this remains as bent as the inactive molecule. It is possible that the transition to the genu-linear state requires that force be exerted on both ends of an integrin, as when it is bound simultaneously to an immobilized ECM ligand and to the cytoskeleton in mechanically stressed tissues (for review see Arnaout et al., 2005).

Materials and methods

Construction, expression, and purification of 1TM-αVβ3

We generated and cloned a new construct encoding human αV residues F1-I967 and β3 residues G1-V696 (with each ending with the fourth putative TM residue, I967 and V696 of αV and β3, respectively; Fig. 1 A) into the pacUW31vector, and the resulting 1TM-αVβ3 pacUW31 vector was used to produce high titer recombinant 1TM-αVβ3 virus, which was used to infect High-Five cells (Invitrogen; Mehta et al., 1998). To assess expression of the soluble recombinant integrin, sterile filtered supernatant was immunoprecipitated with the αVβ3 heterodimer-specific antibody LM609 (Cheresh and Spiro, 1987) conjugated to Affigel-10 beads, and after extraction in SDS-PAGE sample buffer, 200-μl supernatant equivalents were run on 4–12% gradient SDS gels under reducing and nonreducing conditions. After Western blotting, the membrane was blocked with skim milk–Tween and probed with mixed biotinylated 20H9 and 2A5 antibodies, directed against the β3 and αV subunits, respectively, before detection with anti–biotin-HRP and ECL visualization. 62 ng of purified ΔTM-αVβ3 was run in parallel as a standard. The heterodimer could also be confirmed directly by capture ELISA using 17E6 (anti-αV) as capture reagent and AP3 (anti-β3) as detection reagent. The 1TM-αVβ3 receptor was purified for biochemistry and crystallography as previously described for the ΔTM-αVβ3 recombinant (Mehta et al., 1998) except that the mAb 14D9 (Mitjans et al., 1995) was used in affinity chromatography.

Molecular sieve chromatography of purified 1TM-αVβ3

All molecular sieve chromatography analyses were performed as previously described (Adair et al., 2005) using precalibrated Superdex 200 (10/300 GL) columns (GE Healthcare) on an Akta fast protein liquid chromatography system (GE Healthcare) running Unicorn 5.01 software (GE Healthcare) at a flow rate of 0.4 ml min^{-1} at 20°C. The elution profiles were monitored in-line by UV adsorption at 280 nm. TBS buffer (145 mM NaCl and 25 mM Tris-HCl, pH 7.4) containing either Ca and Mg (1 mM MgCl$_2$ and 1 mM CaCl$_2$) or Mn (0.2 mM MnCl$_2$) was used throughout. 5–10 μg of purified ΔTM-αVβ3 or 1TM- αVβ3 was fractionated, and the Stokes radii were derived by substituting their peak elution volumes (Ve) in the fitted standard curve equation (one-phase exponential fit; Prism; GraphPad Software, Inc.). Identity of resolved peaks was formally confirmed by SDS-PAGE and by ELISA using mAb LM609.

Plasmids and stable and transient transfections

Plasmids containing cDNAs encoding WT human full-length αV and β3 were each subcloned in pcDNA3. β-genu deletion (Δβ-genu; residues E^{472}DYRPSQ^{482}), R404A + R633A, and R633A + ΔCD (residues D^{672}-K^{676}) mutants in β3 and G989FF/GAA mutant in αV were made using PCR-based mutagenesis with the QuikChange kit (Agilent Technologies), and authenticity was confirmed by DNA sequencing. Plasmids encoding WT human FN7–10 (P1142 to T1509; provided by H.P. Erickson, Duke University Medical Center, Durham, NC; Leahy et al., 1996), FN9–10 (G1326 to T1509), FN10 (S1417 to T1509), or the high affinity and αVβ3-specific form of FN10 (Richards et al., 2003) were expressed in bacteria and purified as described previously (Aukhil et al., 1993). pcDNA3 plasmids encoding full-length WT αV and β3 were electroporated into K562 cells (American Type Culture Collection; Gupta et al., 2007). Stable K562 clones expressing WT αVβ3 were maintained in Iscove's modified Dulbecco's medium plus 10% heat-inactivated fetal bovine serum, 50 IU/ml penicillin and streptomycin, and 0.5–1.0 mg/ml G418. αV or β3 mutant pcDNA3 plasmids were cotransfected with plasmids encoding the respective WT subunit into HEK 293T cells using Lipofectamine 2000 reagent (Invitrogen) according to the manufacturer's protocol.

Binding of 1TM-αVβ3 to immobilized and soluble ligands

Binding of increasing concentrations (0.001–10 μg/ml) of soluble 1TM-αVβ3 or ΔTM-αVβ3 to immobilized purified FN type III domains 7–10 (FN7–10; at 3 μg/ml) was performed in the absence or presence of cyclic-RGD (cyclo-[Arg-Gly-Asp-D-Phe-(N-Me)Val]-cilengitide) or a control cyclic RAD peptide in 1 mM CaCl$_2$ + 1 mM MgCl$_2$ or 1 mM MnCl$_2$ (in TBS; 0.1% BSA for 3 h at 37°C; Kraft et al., 1999). Binding to uncoated wells was performed in parallel. The bound integrin was detected using biotinylated LM142 mAb (Millipore) at 2 μg/ml and 1:20,000 HRP-labeled anti-biotin antibody (Sigma-Aldrich). Binding of 1TM-αVβ3 to soluble FN7–10 was also performed in solution (Adair et al., 2005) by mixing 1TM-αVβ3 with FN7–10 (in a 1:1.5 stoichiometric ratio) or with native full-length FN (in a 5:1 stoichiometric ratio) for 1 h at 37°C in 145 mM NaCl and 25 mM Tris-HCl, pH 7.4, buffer (TBS) containing 0.2 mM MnCl$_2$ or 1 mM CaCl$_2$ and 1 mM MgCl$_2$. The presence of the 1TM-αVβ3–FN7–10 complex was detected after molecular sieve chromatography, 8% SDS-PAGE analysis, and

Coomassie staining. Using ImageJ software (National Institutes of Health), the measured intensities of the stained 1TM-αVβ3 and FN7–10 gel bands (Fig. 3 C) were 16,514 arbitrary units and 3,468 arbitrary units, respectively, which is a 4.76:1 ratio, yielding a 1:1 stoichiometry, when the molecular masses of 1TM-αVβ3 (180.451 kD) and FN7–10 (39.846 kD) are considered (a ratio of 4.53:1).

Binding of 1TM-αVβ3 to the activation-sensitive mAb AP5

Binding of soluble 1TM-αVβ3 to the Fab fragment of the ligand-inducible binding site mAb AP5 (provided by P.J. Newman, Medical College of Wisconsin, Milwaukee, WI; Honda et al., 1995) was performed by mixing the integrin with the Fab in a 1:1.4 stoichiometric ratio for 30 min on ice in TBS containing 2 mM CaCl$_2$. The complex was detected by molecular sieve chromatography in TBS plus 2 mM CaCl$_2$, and the eluted peaks were analyzed on 12% SDS-PAGE followed by Coomassie staining. Band intensities for the unreduced stained gels corresponding to 1TM-αVβ3 and AP5 Fab (Fig. 3 E) were 7,479.5 arbitrary units (for combined αV and β3 bands) and 2,074.7 arbitrary units, respectively (integrin/Fab ratio of 3.6:1), yielding a 1:1 stoichiometry, with a molecular mass ratio of ~3.6:1 (the calculated molecular mass of Fab is 50 kD).

mAb and soluble ligand binding to cell surface–expressed αVβ3

WT αVβ3–expressing K562 or transiently transfected HEK cells (6 × 10^5 cells per sample) were stained in suspension with 10 μg/ml LM609 and 10 μg/ml AP3 mAbs or 20 μg/ml 17E6 Fab in 100 μl TBS containing 0.5% BSA plus 1 mM CaCl$_2$ + 1 mM MgCl$_2$ or 1 mM MnCl$_2$ for 30 min at RT. After washing, cells were incubated with the fluorophore-conjugated anti–mouse IgG or the anti-Fab antibody at 0°C for 30 min, washed, fixed, and then analyzed by flow cytometry using the CellQuest software (BD). FN binding was assessed in parallel by incubating αVβ3-expressing K562 or batches of transient-transfected HEK 293T with mAb AP3 at 0°C for 45 min and then with 10 μg/ml of Alexa Fluor 488–labeled FN9–10 or FN10 and with Cy3-labeled goat anti–mouse IgG1 in TBS buffer containing 1 mM CaCl$_2$ + 1 mM MgCl$_2$ or 1 mM MnCl$_2$ at 20°C for 30 min. After washing, cells were fixed and analyzed by flow cytometry, and the percentage of AP3-positive cells bound to FN was determined. To assess the effect of unlabeled 17E6 Fab prebound to cellular αVβ3 on subsequent binding of Alexa Fluor 488–FN10, K562 cells were first incubated in the absence or presence of a saturating amount of Fab (at 30 μg/ml) as in the previous section, washed, incubated at 20°C for 30 min with limiting concentrations of WT or high affinity Alexa Fluor 488–FN10 (at 10 μg/ml and 2 μg/ml, respectively), and then analyzed by FACS, and binding was expressed as the percentage of the LM609-positive cells stained in parallel.

Hydrodynamic shift assay for locked integrin

To investigate whether 17E6 Fab binding locked 1TM-αVβ3 in an inactive conformation, 17E6 Fab was incubated in TBS containing 0.2 mM Mn^{2+} (MBB buffer) with 1TM-αVβ3 (1.5:1 Fab/integrin molar ratio) at 20°C for 1.5 h. Aliquots were taken and chromatographed at this time point, and the preformed complex was challenged by adding cilengitide to an end concentration of 10 μM and by incubating at 20°C for 1 h and then resolved by molecular sieve chromatography in MBB buffer. The unligated and 17E6 Fab–ligated ± cilengitide-treated forms of the 1TM-αVβ3 complex were resolved unequivocally as discrete symmetrical peaks on the molecular sieve column. The excess 17E6 Fab, eluting at Kav 0.52, served as an internal standard. Each column run was repeated at least three times, and the mean and SDs for the Kav and elution volumes were calculated and compared using a Student's t test.

Crystallography, structure determination, and refinement

1TM-αVβ3 was crystallized at 4°C by vapor diffusion using the hanging-drop method. The precipitating solution contained 12% PEG 4K, 0.6 M NaCl, 5 mM CaCl$_2$, and 0.1 M Na acetate at pH 5.5. Hexagonal crystals grew over 4–5 d to dimensions of 0.3 × 0.4 × 0.15 mm^3. A native x-ray diffraction dataset from a single cryocooled crystal was collected using the ID19 beamline fitted with a charge-coupled device detector at the Advanced Photon Source Facility. All data were indexed, integrated, and scaled with the HKL2000 program (Otwinowski and Minor, 1997). Data collection statistics are presented in Table I. The structure was solved by molecular replacement using the structure of the ΔTM-αVβ3 as the search model. The model was refined with the crystallography and NMR system (CNS; Brünger et al., 1998) and manually adjusted with O (Jones et al., 1991). After initial simulated annealing, the model was further refined with macromolecular refinement by the maximum-likelihood method (REFMAC; Winn et al., 2001). The complete structure of IE1 and -2, the linker between

Table I. Data collection, refinement, and model statistics

Statistics	Value
Data collection statistics	
Space group	P3221
Unit cell dimensions (Å)	a = b = 130.256, c = 305.982
Resolution range (Å)	50–2.9
Completeness (%)	99.2 (98.5)
Number of unique reflections	66,702 (6,515)
Redundancy	2.9 (2.2)
R_{sym} (%)[a]	8.8 (100)
I/σ	10.5 (100)
Wavelength (Å)	1.0332
Refinement statistics	
Resolution range (Å)	20–2.9
R_{factor} (work set) (%)[b]	24.4
R_{factor} (free set) (%)	28.7
Mean B factors (Å^2)	39.1
Atoms in the model	13,027
Number of GlcNAc	14
Number of Ca^{2+}	6
Model statistics	
(RMSD from ideality)	
Bond lengths (Å)	0.006
Bond angles (°)	1.086

RMSD, root mean square deviation. Values in parentheses are for the highest resolution shell (0.1 Å).

[a]$R_{sym} = \Sigma |I - <I>| / \Sigma I$, where I is the observed intensity and $<I>$ is the mean intensity from multiple observations of symmetry-related reflections.

[b]$R_{factor} = \Sigma_{hkl} |F_o(hkl) - F_c(hkl)| / \Sigma_{hkl} F_o(hkl)$.

PSI and hybrid domains (residues P[51]ES[53]), which were not included in the ΔTM-αVβ3 structure (Protein Data Bank number 1U8C; Xiong et al., 2004), the remaining exofacial residues of the ectodomain (αV's A957-P963 and β3's P691D692), and seven of the eight TM residues were traced and included in the final model. 14 N-linked carbohydrate structures modeled at GlcNAc residues with additional branched sugars, and six Ca ions were also placed. The final model converged to an R$_{work}$ value of 0.24 and R$_{free}$ value of 0.28 (calculated with 5% of reflections omitted from refinement). 97% of the residues from the model fall into favorable or allowed regions of the Ramachandran diagram using the PROCHECK software in CCP4 (Collaborative Computational Project Number 4, 1994).

Fluorescent labeling of 17E6 Fab and FN
The Fab fragment of the αV-specific mAb 17E6 (Mitjans et al., 1995) was prepared by papain digestion followed by anion exchange and size-exclusion chromatography (Andrew, 2002), and its purity was confirmed by SDS-PAGE followed by Coomassie staining. Fab 17E6 and high affinity αVβ3-specific FN10 were labeled with Alexa Fluor 488 N-hydroxysuccinimidyl ester dye using the Alexa Fluor 488 protein labeling kit (Invitrogen) according to the manufacturer's instructions. The final antibody and FN concentrations and the dye to protein molar ratios (F/P) were determined spectrophotometrically, giving F/P molar ratios of ~3–7 (for Fab) and ~1 (for FN9–10 and FN10; FN9 has no lysines). Binding of the fluorophore-labeled FN to αVβ3-expressing cells was evaluated by flow cytometry, and dose–response curves were established to determine the optimal (saturating or subsaturating) concentration of ligand used in subsequent experiments.

Time-correlated single photon counting–FLIM acquisition and analysis
Wells of nonfluorescent Labtek II four-chamber microscope slides (Thermo Fisher Scientific) were coated with poly-L-Lys (Sigma-Aldrich) overnight at 4°C. 25,000–50,000 αVβ3-expressing K562 or HEK 293T cells were transferred in serum-free Iscove's modified Dulbecco's medium to each well and incubated for 30 min at 37°C in a total volume of 200 μl. Nonspecific sites were blocked by incubation with 10% serum-rich medium for 10 min at RT and then washed twice to remove nonadherent cells. Adherent live cells were stained with 20 μg/ml 17E6 labeled with the fluorescence donor Alexa Fluor 488 (Alexa Fluor 488–Fab) in 25 mM Tris, pH 7.4, and 145 mM

NaCl (TBS) containing 1 mM CaCl$_2$, 1 mM CaCl$_2$ and 1 mM MgCl$_2$, or 1 mM MnCl$_2$ for 20 min at 37°C. After two washes, some cells were labeled with 6–12 μM FM4-64 FX (FM) in TBS containing 1 mM CaCl$_2$, 1 mM CaCl$_2$ and 1 mM MgCl$_2$, or 1 mM MnCl$_2$ for 5 min on ice, washed once, immediately fixed with ice-cold 4% paraformaldehyde, washed, and mounted with GVA mount (Invitrogen) under a coverslip. The GVA-mounted slides were kept in the dark and used the next day for FLIM acquisition (Bacskai et al., 2003). In some experiments, adherent K562 expressing WT αVβ3 were pre-incubated with saturating amounts (10 μg/ml) of unlabeled high affinity FN10 followed by the addition of Alexa Fluor 488–Fab and then processed as in the previous section.

FLIM measurements were made on a two-photon microscope (Radiance 2000; Bio-Rad Laboratories) with a femtosecond-pulsed Ti:Sapphire Laser (Mai Tai; Spectra-Physics) at 800-nm excitation. Photons were detected by microchannel plate photomultiplier tube (MCP R3809; Hamamatsu Photonics) with time-correlated single photon counting (SPC830; Becker & Hickl) to measure fluorescent decay profiles. Decay curves were best fit into mono-exponential curves using SPCImage software (version 2.6.1.2711; Becker & Hickl). Lifetimes for multiple cells ($n = 9–14$) for each experimental condition were compared and evaluated for statistically significant differences from control cells (labeled only with donor fluorophore) by analysis of variance with Fisher's post-hoc correction. Percent lifetime decrease, or FRET efficiency (E), was calculated as the difference between the excited state of the donor in absence of acceptor (τ_D) and in presence of acceptor fluorophore (τ_{DA}) according to the equation $E = 1 - \tau_{DA}/\tau_D$. The distance between donor (Fab) and acceptor fluorophores, r, was calculated using the following equation (Duncan et al., 2004): $r = R_0(\tau_D/\tau_{DA} - 1)^{-1/6}$, where R_0 is the Förster radius, the distance at which energy transfer is 50%. We assumed random orientation for the fluorophore (orientation factor, $\kappa^2 = 2/3$) in the Fab molecule. We approximated R_0 as 62 Å based on spectral similarities to the published Alexa Fluor 488–Alexa Fluor 568 pair (Invitrogen).

Online supplemental material
Fig. S1 shows a ribbon diagram of the MIDAS face in the 1TM-αVβ3 and TM-αIIbβ3 structures. Table S1 shows the elution profiles after molecular sieve chromatography of 1TM-αVβ3 or full-length FN alone and in complex. Online supplemental material is available at http://www.jcb.org/cgi/content/full/jcb.200905085/DC1.

References

Adair, B.D., J.P. Xiong, C. Maddock, S.L. Goodman, M.A. Arnaout, and M. Yeager. 2005. Three-dimensional EM structure of the ectodomain of integrin αVβ3 in a complex with fibronectin. *J. Cell Biol.* 168:1109–1118.

Andrew, S.A. 2002. Enzymatic digestion of monoclonal antibodies. *In* The Protein Protocols Handbook. Second edition. J. M. Walker, editor. Humana Press, Totowa, NJ. 1047–1052.

Arnaout, M.A., B. Mahalingam, and J.-P. Xiong. 2005. Integrin structure, allostery, and bidirectional signaling. *Annu. Rev. Cell Dev. Biol.* 21:381–410.

Aukhil, I., P. Joshi, Y. Yan, and H.P. Erickson. 1993. Cell- and heparin-binding domains of the hexabrachion arm identified by tenascin expression proteins. *J. Biol. Chem.* 268:2542–2553.

Bacskai, B.J., J. Skoch, G.A. Hickey, R. Allen, and B.T. Hyman. 2003. Fluorescence resonance energy transfer determinations using multiphoton fluorescence lifetime imaging microscopy to characterize amyloid-beta plaques. *J. Biomed. Opt.* 8:368–375.

Brünger, A.T., P.D. Adams, and L.M. Rice. 1998. Recent developments for the efficient crystallographic refinement of macromolecular structures. *Curr. Opin. Struct. Biol.* 8:606–611.

Cheresh, D.A., and R.C. Spiro. 1987. Biosynthetic and functional properties of an Arg-Gly-Asp-directed receptor involved in human melanoma cell attachment to vitronectin, fibrinogen, and von Willebrand factor. *J. Biol. Chem.* 262:17703–17711.

Chigaev, A., A.M. Blenc, J.V. Braaten, N. Kumaraswamy, C.L. Kepley, R.P. Andrews, J.M. Oliver, B.S. Edwards, E.R. Prossnitz, R.S. Larson, and

L.A. Sklar. 2001. Real time analysis of the affinity regulation of alpha 4-integrin. The physiologically activated receptor is intermediate in affinity between resting and Mn(2+) or antibody activation. *J. Biol. Chem.* 276:48670–48678.

Chigaev, A., T. Buranda, D.C. Dwyer, E.R. Prossnitz, and L.A. Sklar. 2003. FRET detection of cellular alpha4-integrin conformational activation. *Biophys. J.* 85:3951–3962.

Chigaev, A., A. Waller, O. Amit, L. Halip, C.G. Bologa, and L.A. Sklar. 2009. Real-time analysis of conformation-sensitive antibody binding provides new insights into integrin conformational regulation. *J. Biol. Chem.* 284:14337–14346.

Collaborative Computational Project Number 4. 1994. The CCP4 suite: programs for protein crystallography. *Acta Crystallogr. D Biol. Crystallogr.* 50:760–763.

Coutinho, A., C. García, J. González-Rodríguez, and M.P. Lillo. 2007. Conformational changes in human integrin alphaIIbbeta3 after platelet activation, monitored by FRET. *Biophys. Chem.* 130:76–87.

Duncan, R.R., A. Bergmann, M.A. Cousin, D.K. Apps, and M.J. Shipston. 2004. Multi-dimensional time-correlated single photon counting (TCSPC) fluorescence lifetime imaging microscopy (FLIM) to detect FRET in cells. *J. Microsc.* 215:1–12.

Faccio, R., M. Grano, S. Colucci, A. Villa, G. Giannelli, V. Quaranta, and A. Zallone. 2002. Localization and possible role of two different alpha v beta 3 integrin conformations in resting and resorbing osteoclasts. *J. Cell Sci.* 115:2919–2929.

Fiser, A., and A. Sali. 2003. Modeller: generation and refinement of homology-based protein structure models. *Methods Enzymol.* 374:461–491.

Giepmans, B.N., S.R. Adams, M.H. Ellisman, and R.Y. Tsien. 2006. The fluorescent toolbox for assessing protein location and function. *Science.* 312:217–224.

Gupta, V., A. Gylling, J.L. Alonso, T. Sugimori, P. Ianakiev, J.P. Xiong, and M.A. Arnaout. 2007. The beta-tail domain (betaTD) regulates physiologic ligand binding to integrin CD11b/CD18. *Blood.* 109:3513–3520.

Honda, S., Y. Tomiyama, A.J. Pelletier, D. Annis, Y. Honda, R. Orchekowski, Z. Ruggeri, and T.J. Kunicki. 1995. Topography of ligand-induced binding sites, including a novel cation-sensitive epitope (AP5) at the amino terminus, of the human integrin beta 3 subunit. *J. Biol. Chem.* 270:11947–11954.

Hynes, R.O. 2002. Integrins: bidirectional, allosteric signaling machines. *Cell.* 110:673–687.

Jares-Erijman, E.A., and T.M. Jovin. 2003. FRET imaging. *Nat. Biotechnol.* 21:1387–1395.

Jones, T.A., J.Y. Zou, S.W. Cowan, and M. Kjeldgaard. 1991. Improved methods for building protein models in electron density maps and the location of errors in these models. *Acta Crystallogr. A.* 47:110–119.

Kamata, T., M. Handa, Y. Sato, Y. Ikeda, and S. Aiso. 2005. Membrane-proximal alpha/beta stalk interactions differentially regulate integrin activation. *J. Biol. Chem.* 280:24775–24783.

Kim, M., C.V. Carman, and T.A. Springer. 2003. Bidirectional transmembrane signaling by cytoplasmic domain separation in integrins. *Science.* 301:1720–1725.

Kraft, S., B. Diefenbach, R. Mehta, A. Jonczyk, G.A. Luckenbach, and S.L. Goodman. 1999. Definition of an unexpected ligand recognition motif for alphav beta6 integrin. *J. Biol. Chem.* 274:1979–1985.

Lau, T.L., C. Kim, M.H. Ginsberg, and T.S. Ulmer. 2009. The structure of the integrin alphaIIbbeta3 transmembrane complex explains integrin transmembrane signalling. *EMBO J.* 28:1351–1361.

Leahy, D.J., I. Aukhil, and H.P. Erickson. 1996. 2.0 A crystal structure of a four-domain segment of human fibronectin encompassing the RGD loop and synergy region. *Cell.* 84:155–164.

Lee, J.O., L.A. Bankston, M.A. Arnaout, and R.C. Liddington. 1995. Two conformations of the integrin A-domain (I-domain): a pathway for activation? *Structure.* 3:1333–1340.

Matsumoto, A., T. Kamata, J. Takagi, K. Iwasaki, and K. Yura. 2008. Key interactions in integrin ectodomain responsible for global conformational change detected by elastic network normal-mode analysis. *Biophys. J.* 95:2895–2908.

Mehta, R.J., B. Diefenbach, A. Brown, E. Cullen, A. Jonczyk, D. Güssow, G.A. Luckenbach, and S.L. Goodman. 1998. Transmembrane-truncated alphavbeta3 integrin retains high affinity for ligand binding: evidence for an 'inside-out' suppressor? *Biochem. J.* 330:861–869.

Mitjans, F., D. Sander, J. Adán, A. Sutter, J.M. Martinez, C.S. Jäggle, J.M. Moyano, H.G. Kreysch, J. Piulats, and S.L. Goodman. 1995. An anti-alpha v-integrin antibody that blocks integrin function inhibits the development of a human melanoma in nude mice. *J. Cell Sci.* 108:2825–2838.

Mould, A.P., J.A. Askari, and M.J. Humphries. 2000. Molecular basis of ligand recognition by integrin alpha 5beta 1. I. Specificity of ligand binding is determined by amino acid sequences in the second and third NH2-terminal repeats of the alpha subunit. *J. Biol. Chem.* 275:20324–20336.

Mould, A.P., S.J. Barton, J.A. Askari, P.A. McEwan, P.A. Buckley, S.E. Craig, and M.J. Humphries. 2003. Conformational changes in the integrin beta A domain provide a mechanism for signal transduction via hybrid domain movement. *J. Biol. Chem.* 278:17028–17035.

Otwinowski, Z., and W. Minor. 1997. Processing of X-ray diffraction data collected in oscillation mode. In *Macromolecular Crystallography*. Methods in Enzymology, vol. 276. J.N. Abelson, M.I. Simon, C.W. Carter Jr., and R.M. Sweet, editors. Academic Press, New York. 307–326.

Perutz, M.F. 1989. Mechanisms of cooperativity and allosteric regulation in proteins. *Q. Rev. Biophys.* 22:139–237.

Pesho, M.M., K. Bledzka, L. Michalec, C.S. Cierniewski, and E.F. Plow. 2006. The specificity and function of the metal-binding sites in the integrin beta3 A-domain. *J. Biol. Chem.* 281:23034–23041.

Pettersen, E.F., T.D. Goddard, C.C. Huang, G.S. Couch, D.M. Greenblatt, E.C. Meng, and T.E. Ferrin. 2004. UCSF Chimera—a visualization system for exploratory research and analysis. *J. Comput. Chem.* 25:1605–1612.

Puklin-Faucher, E., M. Gao, K. Schulten, and V. Vogel. 2006. How the headpiece hinge angle is opened: new insights into the dynamics of integrin activation. *J. Cell Biol.* 175:349–360.

Richards, J., M. Miller, J. Abend, A. Koide, S. Koide, and S. Dewhurst. 2003. Engineered fibronectin type III domain with a RGDWXE sequence binds with enhanced affinity and specificity to human alphavbeta3 integrin. *J. Mol. Biol.* 326:1475–1488.

Rocco, M., C. Rosano, J.W. Weisel, D.A. Horita, and R.R. Hantgan. 2008. Integrin conformational regulation: uncoupling extension/tail separation from changes in the head region by a multiresolution approach. *Structure.* 16:954–964.

Rohl, C.A., C.E. Strauss, K.M. Misura, and D. Baker. 2004. Protein structure prediction using Rosetta. *Methods Enzymol.* 383:66–93.

Senes, A., D.E. Engel, and W.F. DeGrado. 2004. Folding of helical membrane proteins: the role of polar, GxxxG-like and proline motifs. *Curr. Opin. Struct. Biol.* 14:465–479.

Stetefeld, J., U. Mayer, R. Timpl, and R. Huber. 1996. Crystal structure of three consecutive laminin-type epidermal growth factor-like (LE) modules of laminin gamma1 chain harboring the nidogen binding site. *J. Mol. Biol.* 257:644–657.

Takagi, J., B.M. Petre, T. Walz, and T.A. Springer. 2002. Global conformational rearrangements in integrin extracellular domains in outside-in and inside-out signaling. *Cell.* 110:599–11.

Takagi, J., K. Strokovich, T.A. Springer, and T. Walz. 2003. Structure of integrin alpha5beta1 in complex with fibronectin. *EMBO J.* 22:4607–4615.

Wegener, K.L., A.W. Partridge, J. Han, A.R. Pickford, R.C. Liddington, M.H. Ginsberg, and I.D. Campbell. 2007. Structural basis of integrin activation by talin. *Cell.* 128:171–182.

Winn, M.D., M.N. Isupov, and G.N. Murshudov. 2001. Use of TLS parameters to model anisotropic displacements in macromolecular refinement. *Acta Crystallogr. D Biol. Crystallogr.* 57:122–133.

Wouters, M.A., I. Rigoutsos, C.K. Chu, L.L. Feng, D.B. Sparrow, and S.L. Dunwoodie. 2005. Evolution of distinct EGF domains with specific functions. *Protein Sci.* 14:1091–1103.

Xiao, T., J. Takagi, B.S. Coller, J.H. Wang, and T.A. Springer. 2004. Structural basis for allostery in integrins and binding to fibrinogen-mimetic therapeutics. *Nature.* 432:59–67.

Xiong, J.P., T. Stehle, B. Diefenbach, R. Zhang, R. Dunker, D.L. Scott, A. Joachimiak, S.L. Goodman, and M.A. Arnaout. 2001. Crystal structure of the extracellular segment of integrin alpha Vbeta3. *Science.* 294:339–345.

Xiong, J.P., T. Stehle, R. Zhang, A. Joachimiak, M. Frech, S.L. Goodman, and M.A. Arnaout. 2002. Crystal structure of the extracellular segment of integrin alpha Vbeta3 in complex with an Arg-Gly-Asp ligand. *Science.* 296:151–155.

Xiong, J.P., T. Stehle, S.L. Goodman, and M.A. Arnaout. 2003. New insights into the structural basis of integrin activation. *Blood.* 102:1155–1159.

Xiong, J.P., T. Stehle, S.L. Goodman, and M.A. Arnaout. 2004. A novel adaptation of the integrin PSI domain revealed from its crystal structure. *J. Biol. Chem.* 279:40252–40254.

Ye, F., J. Liu, H. Winkler, and K.A. Taylor. 2008. Integrin alpha IIb beta 3 in a membrane environment remains the same height after Mn2+ activation when observed by cryoelectron tomography. *J. Mol. Biol.* 378:976–986.

Zhu, J., B. Boylan, B.H. Luo, P.J. Newman, and T.A. Springer. 2007. Tests of the extension and deadbolt models of integrin activation. *J. Biol. Chem.* 282:11914–11920.

Zhu, J., B.H. Luo, T. Xiao, C. Zhang, N. Nishida, and T.A. Springer. 2008. Structure of a complete integrin ectodomain in a physiologic resting state and activation and deactivation by applied forces. *Mol. Cell.* 32:849–861.

Zhu, J., B.H. Luo, P. Barth, J. Schonbrun, D. Baker, and T.A. Springer. 2009. The structure of a receptor with two associating transmembrane domains on the cell surface: integrin alphaIIbbeta3. *Mol. Cell.* 34:234–249.